frontiers | Frontiers in Bioengineering and Biotechnology

TYPE Original Research
PUBLISHED 18 October 2022
DOI 10.3389/fbioe.2022.1023090

OPEN ACCESS

EDITED BY
Shuaifei Zhao,
Deakin University, Australia

REVIEWED BY
Chongqing Wang,
Zhengzhou University, China
Nuo Yu,
Donghua University, China

*CORRESPONDENCE
Shuangchen Ruan,
scruan@sztu.edu.cn

SPECIALTY SECTION
This article was submitted to Bioprocess Engineering, a section of the journal Frontiers in Bioengineering and Biotechnology

RECEIVED 19 August 2022
ACCEPTED 04 October 2022
PUBLISHED 18 October 2022

CITATION
Wu M, He S, Ha E, Hu J and Ruan S (2022), A facile synthesis of PEGylated $Cu_2O@SiO_2/MnO_2$ nanocomposite as efficient photo–Fenton–like catalysts for methylene blue treatment.
Front. Bioeng. Biotechnol. 10:1023090.
doi: 10.3389/fbioe.2022.1023090

A facile synthesis of PEGylated $Cu_2O@SiO_2/MnO_2$ nanocomposite as efficient photo–Fenton–like catalysts for methylene blue treatment

Mingzhou Wu[1,2], Shuqing He[2], Enna Ha[2], Junqing Hu[2] and Shuangchen Ruan[1,3]*

[1]Key Laboratory of Optoelectronic Devices and Systems of Ministry of Education and Guangdong Province, Shenzhen Key Laboratory of Laser Engineering, College of Physics and Optoelectronic Engineering, Shenzhen University, Shenzhen, China, [2]College of Health Science and Environmental Engineering, Shenzhen Technology University, Shenzhen, China, [3]Sino-German College of Intelligent Manufacturing, Shenzhen Technology University, Shenzhen, China

The removal of toxic organic dyes from wastewater has received much attention from the perspective of environmental protection. Metal oxides see wide use in pollutant degradation due to their chemical stability, low cost, and broader light absorption spectrum. In this work, a Cu_2O–centered nanocomposite $Cu_2O@SiO_2/MnO_2$–PEG with an average diameter of 52 nm was prepared for the first time *via* a wet chemical route. In addition, highly dispersed MnO_2 particles and PEG modification were realized simultaneously in one step, meanwhile, Cu_2O was successfully protected under a dense SiO_2 shell against oxidation. The obtained $Cu_2O@SiO_2/MnO_2$–PEG showed excellent and stable photo–Fenton–like catalytic activity, attributed to integration of visible light–responsive Cu_2O and H_2O_2–responsive MnO_2. A degradation rate of 92.5% and a rate constant of 0.086 min^{-1} were obtained for methylene blue (MB) degradation in the presence of H_2O_2 under visible light for 30 min. Additionally, large amounts of •OH and $^1O_2$ species played active roles in MB degradation. Considering the enhanced degradation of MB, this stable composite provides an efficient catalytic system for the selective removal of organic contaminants in wastewater.

KEYWORDS

$Cu_2O@SiO_2/MnO_2$–$_{PEG}$, wastewater treatment, photocatalysis, photo–Fenton–like property, methylene blue

1 Introduction

Synthetic dyes and pigments like MB, Rhodamine B (RhB) and methyl orange (MO) used in the pharmaceutical, tannery, and textile industries are common sources of water pollution due to their complex aromatic molecular structure (Mohammadzadeh et al., 2020; Fan et al., 2021). This is especially true for textile manufacturing, as 10–50% of dye losses are discharged into the effluent (Uddin et al., 2021). Various physicochemical treatment strategies, including membrane filtration (Mohammed et al., 2020; Ni et al., 2022; Xiong et al., 2022), physical adsorption (Qiu et al., 2020; Huang et al., 2022), biological degradation (Deng et al., 2021), and advanced oxidation processes (AOPs) have been reported (Wang et al., 2021a; Li et al., 2022b). However, traditional treatments are hampered by recycling and economic costs. Using environmentally friendly, rapidly oxidative, and highly efficient pollutant elimination, photocatalysis and Fenton reactions are employed as common methods for pollutant elimination due to the oxidation activities of hydroxyl radicals (•OH) and superoxide anions ($O_2^{\bullet -}$) (Zhang et al., 2021a; Wang et al., 2021b; Yang et al., 2022a).

Previous studies indicated that semiconductor materials such as metal oxides and transition metal sulfides are common photocatalysts. Metal–oxide–related photocatalysts underwent three generations, single–component materials, multiple–component materials, and solid substrate immobilized materials (Anwer et al., 2019; Ivanets et al., 2021). Materials with photo-sensitive reaction and Fenton-like reaction have been widely reported in the area of catalysis and bioapplication, such as metals (Yu et al., 2018), organics (Qiu et al., 2022), and metal-organic frameworks (Yu et al., 2021a; Liu et al., 2022; Yu et al., 2022). Cuprous oxide (Cu_2O) is a promising p–type semiconductor with a 2.1 eV bandgap and displays a wide absorption band in the visible light region (Yang et al., 2016). Moreover, considering its inexpensive and convenient synthesis, abundant resources, and non–toxicity, Cu_2O has been explored as an ideal candidate for photocatalysis (Wu et al., 2012). However, nanosized Cu_2O particles readily oxidize in air or humid conditions, which significantly limits their application (Zhai et al., 2014). To stabilize Cu_2O and improve its catalytic activities, reductive components have been utilized. For example, Wang et al. reported stable Cu_2O nanoparticles supported on reduced graphene oxide (Cu_2O/RGO), which showed excellent activity and recyclability towards Sonogashira cross–coupling of aryl halides with phenylacetylene and Ullmann coupling of phenols with aryl halides (Zhai et al., 2014; Wang et al., 2017a). Recently, a Ag–Cu_2O composite film and a Ag/Cu_2O heterojunction were applied in dye degradation reported by Yu et al. and Li et al., respectively. They illustrated that Ag could improve the photocatalytic performance by facilitating photoelectron transfer and accelerating the separation of photoelectron–holes in Cu_2O. MB degradation rate of over 95.1% was obtained over Ag–Cu_2O composite film (Yu et al., 2021b). Similarly, methyl orange (MO) was almost complete eliminated within 40 min under visible light irradiation using Ag/Cu_2O (Li et al., 2022a). Moreover, hybrid Cu_2O–Cu cubes exhibited visible–light–driven degradation against MO and rhodamine B (RhB) in the presence of H_2O_2 as a sacrificial scavenger. Due to the efficient separation of electron–hole pairs and improved charge transfer, Cu_2O–Cu exhibits superior photocatalytic performance (Alp, 2021). However, the reductive component in composite materials is often sensitive to H_2O_2–conducted degradation systems.

The improvements of metal oxides related composite materials are commonly attributed to electron–hole separation facilitation, which promoted active species production (•OH, $O_2^{\bullet -}$ etc.) during degradation (Hao et al., 2021). Could additional O_2 improve the degradation efficiency? Herein, we sought to develop an ideal material functional in both O_2 improvement and Cu_2O protection. MnO_2 is well known for O_2 production from H_2O_2 via Fenton–like reaction for water treatment, biological antibacterial, and anticancer applications (Wang et al., 2018; Sun et al., 2021; Yang et al., 2021; Gemeay et al., 2008) reported polyaniline/MnO_2 composites in the oxidative decolorization of organic dyes with H_2O_2. Based on H_2O_2 bubble generation over Fe_3O_4@MnO_2, a removal efficiency of 99% was reached *via* advanced oxidation and adsorptive bubble separation (Kang et al., 2019). Recently, Jiao et al. synthesized MnO_2 nanoparticle–loaded poly (amidoxime–hydroxamic acid)–modified microcrystalline cellulose (pAHA–MCC@MnO_2). The birnessite–like MnO_2 nanoparticles on the pAHA–MCC microrod surfaces played a vital role in MB due to advanced Fenton–like catalysis (Jiao et al., 2021). Therefore, combining Cu_2O and MnO_2 might develop an efficient catalyst for MB degradation in the presence of both visible light and H_2O_2.

In this work, a novel composite catalyst Cu_2O@SiO_2/MnO_2–PEG was designed as photo–Fenton–like catalysts by introducing a highly dispersed ultrafine MnO_2 and a dense SiO_2 shell. This creative development sought to protect Cu_2O from instability coupled with producing MnO_2 from $KMnO_4$ and PEG, which endow the sample with photo–Fenton–like catalytic activity. The synthetic procedure occurs at lower temperatures and with low energy consumption. The catalytic performance of Cu_2O@SiO_2/MnO_2–PEG was subsequently evaluated by degrading MB dye in the presence of H_2O_2 under visible light irradiation. Furthermore, the mechanism for MB degradation was investigated to illustrate the roles of each component during the reaction.

2 Materials and methods

2.1 Materials

Copper (II) acetate and ammonium molybdate were obtained from Macklin Biochemical Co., Ltd. Tetraethyl orthosilicate (TEOS) and polyethylene glycol 600 (PEG-600) were purchased from Aladdin Industrial Corporation. Deionized water was purified using Milli-Q system (Millipore Co., United States). Absolute ethyl alcohol and 30% hydrogen peroxide were sourced from Sinopharm Chemical Reagent Co., Ltd. Phosphate buffer saline (PBS) was sourced from Hyclone. All the reagents were used without further purification.

2.2 Synthesis of Cu_2O nanospheres

Cu_2O was synthesized by a modified method, which was reported in the literatures (Zhang et al., 2011; An et al., 2018). In the procedure for Cu_2O synthesis, 80 mg of copper acetate and 1 g of poly−(vinylpyrrolidone) (PVP, Mw 10,000) were dissolved in 30.0 mL of glycol at 70°C. After intensive stirring for 2 h, 10.0 mL of sodium hydroxide (2 mol L^{-1}) was added into the above mixture. Gradually, the transparent green solution turned blue, indicating the formatifon of copper hydrate. And then 0.5 h latter, 10.0 mL of ascorbic acid (AA) solution (0.15 mol L^{-1}) was quickly introduced into the solution to reduce the Cu (II) ions. In order to proceed nanocrystal growth, the turbid yellow suspension was kept in the oil bath with stirring for another 0.5 h. And then it was centrifuged at 10000 rpm for 5 min with decanting the top solution. Finally, the precipitate was washed with distilled water for three times. The obtained Cu_2O nanoparticles were re-dispersed in 5 mL of ethanol for further use.

2.3 Synthesis of $Cu_2O@SiO_2$

5 mL of the obtained Cu_2O ethanol dispersion were dispersed in a solution (57 mL of ethanol/11 mL of water, 0.4 g of PVP) with ultra−sonication. After stirring for 15 min, the as−prepared TEOS ethanol solution (0.15 mL of TEOS, 1.5 mL of ethanol) was added to the above dispersion and stirred for additional 15 min. Then, 1.0 mL of 0.1 M NaOH aqueous solution was added drop−wisely within 5 min at room temperature with stirring. After 14 h, $Cu_2O@SiO_2$ were collected by centrifugation (8000 rpm, 5 min) and washed twice with 1:2 volume ratio of water and ethanol. Finally, the sample was re−dispersed in 5 mL ethanol.

2.4 Synthesis of $Cu_2O@SiO_2/MnO_2$−PEG

The above $Cu_2O@SiO_2$ was dispersed in 75 mL water using sonication. At room temperature, aqueous PEG (Mw: 600, 1.5 mL, 5 mg mL^{-1}) was added into the suspension and mixed for 30 min. After the gentle addition of aqueous $KMnO_4$ (1.875 mL, 200 μg mL^{-1}), the mixture was stirred for 30 min. Subsequently, the mixture was centrifuged at 8000 rpm. The product washed with DI water and ethanol for three times.

2.5 Characterization

The morphology and structural characterization were performed on a scanning electron microscope (SEM, Hitachi S-4800, Japan) and a transmission electron microscope (TEM, JEM-2100F, Japan). X-ray diffraction (XRD) was performed on an Empyrean X-ray diffractometer (PANalytical, Netherlands). UV−vis−NIR spectra were recorded from 200 nm to 800 nm on a UV−vis−NIR spectrophotometer (LAMBDA 1050+, PerkinElmer). An ESCALab 250Xi (Thermo Scientific) spectrometer was used to measure X-ray photoelectron spectroscopy (XPS). An INVENIO S spectrophotometer (Bruker) was operated to acquire the Fourier transform infrared (FTIR) spectra. Photoluminescence (PL) spectra (Ex = 490 nm) were collected on FS 5 fluorescence spectrometer (Edinburgh Instruments) equipped with Xe lamp. The Brunauer-Emmett-Teller (BET) surface areas were obtained using the nitrogen adsorption−desorption isotherms determined at the temperature of liquid nitrogen on an automatic analyzer (Autosorb-iQ-MP, Quantachrome, United States). Electron paramagnetic resonance (EPR) spectra were recorded on a Bruker EMXnano.

2.6 Photo−Fenton−like catalytic degradation of methylene blue

The photo−Fenton−like catalytic performances were carried out in a 250 mL quartz beaker equipped with recirculation cooler in a light protective box. The visible light was created by a 300 W xenon lamp through an UV−cut off filter ($\geq$ 420 nm). Typically, 100 mL, 10 mg L^{-1} of MB dye and 0.015 g of $Cu_2O@SiO_2/MnO_2$−PEG was loaded in the beaker. After stirring for 30 min to establish the adsorption/desorption equilibrium, the mixture was exposed to the visible light and subsequently added a known concentration of H_2O_2. Samples of the reaction mixture were taken every 15 min intervals in the first 2 h, and 30 min intervals in the following 1 h. Batch experiments included catalyst dosage, concentration of MB, effects of ion species. Furthermore, solution pH variation and the types of reactive species were studied. The purpose was to investigate the catalytic activity and degradation mechanism of MB by $Cu_2O@SiO_2/MnO_2$−PEG.

By using the external syringe−driven filter, the concentration of MB was investigated *via* a PerkinElmer Lambda 1050 + UV−Vis spectrophotometer. The quality of MB was obtained according to the maximum absorbance at a wavelength of 663 nm. The conversion efficiency for MB was calculated from Eq. 1:

$$\%\text{MB dye} = C_t/C_0 \times 100\% \tag{1}$$

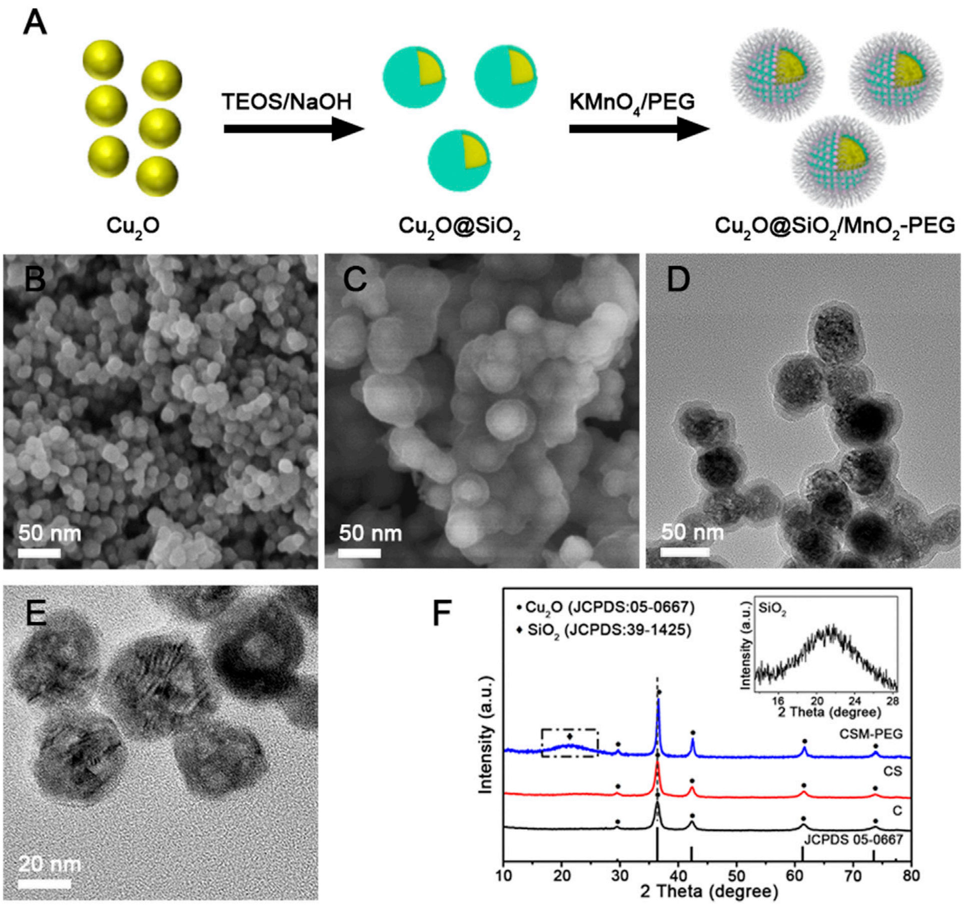

FIGURE 1
(A) The synthesis process of $Cu_2O@SiO_2/MnO_2$–PEG. **(B,C)** SEM and TEM images of Cu_2O. **(D,E)** SEM and TEM images of $Cu_2O@SiO_2/MnO_2$–PEG. **(F)** XRD patterns for Cu_2O (C), $Cu_2O@SiO_2$ (CS), and $Cu_2O@SiO_2/MnO_2$–PEG (CSM–PEG). Insert: XRD patterns for SiO_2.

The degradation reaction rate constant k was calculated according to the pseudo-first-order degradation reaction using Eq. 2:

$$C_t = C_0 e^{-kt} \tag{2}$$

in which C_0 and C_t are the concentrations of MB before and after exposure for a time duration "t", respectively.

3 Results and discussion

3.1 Characterization of prepared $Cu_2O@SiO_2/MnO_2$–PEG

The synthesis process of $Cu_2O@SiO_2/MnO_2$–PEG was shown in Figure 1A. SEM and TEM tests further studied the morphology of pure Cu_2O and $Cu_2O@SiO_2/MnO_2$–PEG. As shown in Figures 1B,E, Cu_2O displayed a nearly spherical structure with a diameter of approximately 40 nm. Supplementary Figure S1 gives the size distribution histogram of Cu_2O in the supporting information. Notably, Figure 1C,D clearly show the core–shell $Cu_2O@SiO_2/MnO_2$–PEG nanostructure with a 7 nm thick uniform SiO_2 shell on the Cu_2O. The existence of such a dense SiO_2 coating protects Cu_2O from instability. According to SEM and TEM images, the $Cu_2O@SiO_2/MnO_2$–PEG particles have diameters of approximately 52 nm. Moreover, Figure 1F shows the X–ray diffraction (XRD) patterns, in which the XRD for pure Cu_2O (marked as "C") agreed with standard Cu_2O (JCPDS card no. 05–0667). Both $Cu_2O@SiO_2$ (marked as "CS") and $Cu_2O@SiO_2/MnO_2$–PEG (marked as "CSM–PEG") exhibit a broad peak due to amorphous SiO_2 with a characteristic peak at 21.4°, which matched the standard SiO_2 (JCPDS card no. 39–1425). Remarkably, due to minimal MnO_2 loading, it was difficult to verify the exhibition of the MnO_2 component either in electron microscope images or in the XRD patterns. It reveals that Cu_2O was successfully coated by SiO_2 shell.

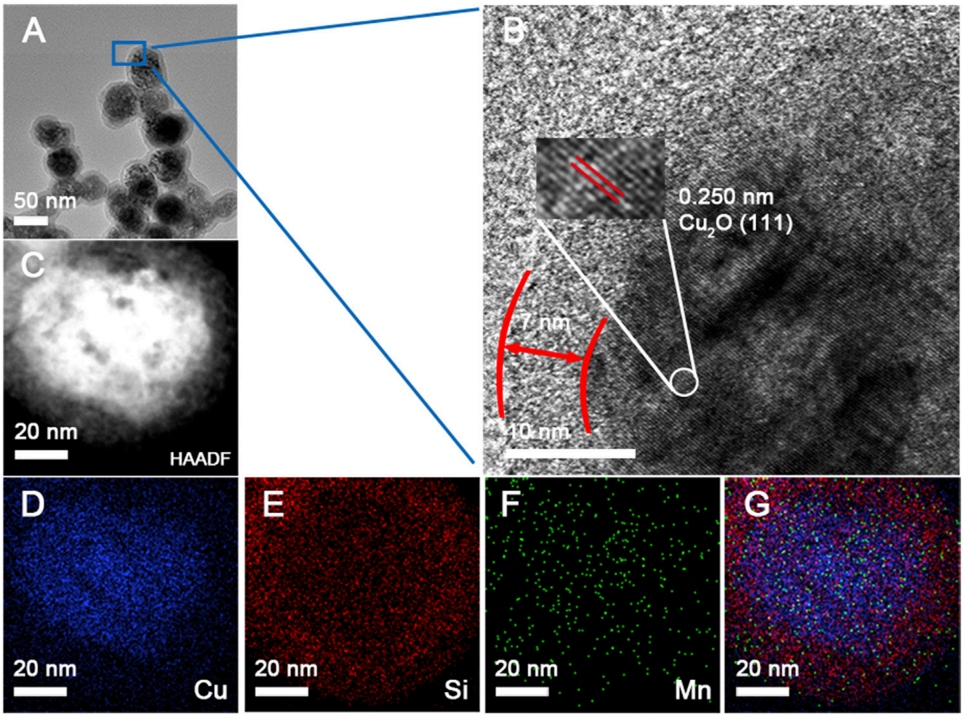

FIGURE 2
(A,B) TEM and HRTEM images of $Cu_2O@SiO_2/MnO_2$–PEG. **(C–G)** HAADF–STEM image and element mapping of Cu, Si, and Mn, as well as overall maps for the $Cu_2O@SiO_2/MnO_2$–PEG composite.

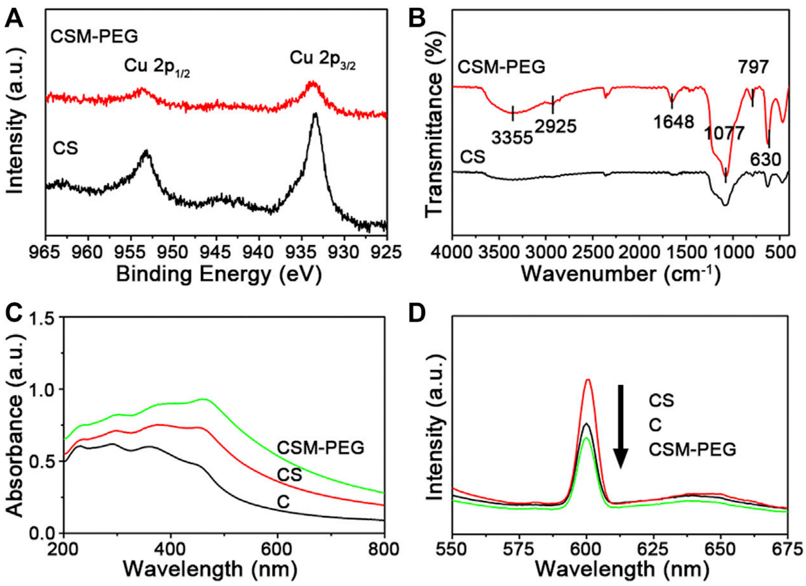

FIGURE 3
(A) Cu 2p XPS spectra for $Cu_2O@SiO_2$ and $Cu_2O@SiO_2/MnO_2$–PEG. **(B)** FT–IR spectra for $Cu_2O@SiO_2$ and $Cu_2O@SiO_2/MnO_2$–PEG. **(C)** UV–Vis spectra for Cu_2O, $Cu_2O@SiO_2$, and $Cu_2O@SiO_2/MnO_2$–PEG dispersed in water. **(D)** PL spectra of Cu_2O, $Cu_2O@SiO_2$, and $Cu_2O@SiO_2/MnO_2$–PEG suspension.

As shown in Figures 2A,B, the lattice fringes of Cu_2O and the interfaces of Cu_2O and SiO_2 were resolved clearly in the high−resolution TEM (HRTEM). The set of lattices with interlayer spacings of 0.250 nm corresponded to the (111) planes of Cu_2O. Furthermore, elemental mapping investigated the homogeneous distribution of Cu, Si, and Mn in the $Cu_2O@SiO_2/MnO_2$−PEG composite. Figure 2C−G verify that Cu_2O is coated entirely by SiO_2 and that MnO_2 uniformly incorporated throughout the SiO_2 shell, which suggested successful loading of MnO_2 on SiO_2. It is worth mentioning the special core−shell structure enabled the integration of MnO_2 and unstable Cu_2O.

X−ray photoelectron spectroscopy (XPS), as a sensitive characterization technique, determined the amount of each element in the sample. Herein, XPS spectra for $Cu_2O@SiO_2$ and $Cu_2O@SiO_2/MnO_2$−PEG were observed. The Cu 2p spectrum shown in Figure 3A contains Cu $2p_{1/2}$ and Cu $2p_{3/2}$. Because of the filled 3 days shells in Cu^+, no charge transfer between Cu^+ compounds and metallic Cu occurred. Herein, the absence of strong satellite peaks located at 6 eV and 8 eV above the principal Cu 2p line confirmed Cu(I), and ruled out the possibility of a CuO phase in $Cu_2O@SiO_2$ and $Cu_2O@SiO_2/MnO_2$−PEG (Colón et al., 2006). As a result, Cu_2O nanoparticles were sufficiently protected by SiO_2. Moreover, the peaks at 933.2 eV and 933.5 eV correspond to Cu $2p_{3/2}$ (Ghodselahi et al., 2008). Compared with $Cu_2O@SiO_2$, the characteristic peaks for Cu^+ in $Cu_2O@SiO_2/MnO_2$−PEG broadened and attributed to the abundant PEG chain on its surface. As shown in Figure 3B, FTIR peaks observed at 3355 cm^{-1}, 2858–2946 cm^{-1}, and 1077 cm^{-1} were attributed to characteristic −OH, $-CH_2$, and C−O−C vibrations, respectively. Furthermore, the peak centered at 1648 cm^{-1} was assigned to bending and stretching vibrations of the surface OH groups stemming from PEG modifications on the $Cu_2O@SiO_2/MnO_2$ surface (Caccamo and Magazù, 2017; Singh et al., 2020; Ghauri et al., 2022). Additionally, the broad absorption peaks at approximately 1063 cm^{-1} and 797 cm^{-1} corresponded to the asymmetric stretching mode of Si−O−Si and Si−O−C bonds and symmetric stretching vibration of Si−O bonds, respectively (Cheng et al., 2022). The band at 630 cm^{-1} was coincident with the optically active lattice vibration of Cu−O in Cu_2O (Zhang et al., 2009; Hao et al., 2021). As a result, the characteristic peaks observed for PEG, SiO_2, and Cu_2O in the FTIR spectra confirmed the successful preparation of PEGylated $Cu_2O@SiO_2/MnO_2$ and agreed with TEM and XPS data. In addition, wavelengths of visible light range from 770 nm to 350 nm, corresponding photon energy from 1.61 eV to 3.54 eV. However, photon energy band gap of SiO_2 is approximately 9.3 eV (Weinberg et al., 1979), which is much higher than 3.54 eV, resulting in almost no absorption of visible light. Consequently, it is demonstrated that SiO_2 coating will not inhibit Cu_2O from photosensitivity. The efficient photocatalytic activity commonly occurs with the complex generation of electron−hole pairs within a semiconductor. UV−Vis spectra for Cu_2O, $Cu_2O@SiO_2$, and $Cu_2O@SiO_2/MnO_2$−PEG were shown in Figure 3C. The peak intensity at 465 nm increased, followed by the SiO_2 coating, and MnO_2−PEG incorporation. The irradiation energy accelerated the generation of electron−hole pairs in $Cu_2O@SiO_2/MnO_2$−PEG under visible light, which increased photocatalytic efficiency. Photoluminescence (PL) spectra of Cu_2O, $Cu_2O@SiO_2$, and $Cu_2O@SiO_2/MnO_2$−PEG investigated the migration and separation efficiency of the photo−generated charge carriers. As shown in Figure 3D, the emission intensity at 600 nm decreased in the following order, $Cu_2O@SiO_2$ > Cu_2O > $Cu_2O@SiO_2/MnO_2$−PEG. The weakened emission intensity of $Cu_2O@SiO_2/MnO_2$−PEG indicated low recombination of the electron−hole pairs in VB and CB due to MnO_2. Thus, the effective separation of electron−hole pairs improved the photocatalytic properties (He et al., 2017; Hao et al., 2021).

3.2 Photocatalytic performance

To evaluate the photo−Fenton−like catalytic performance of $Cu_2O@SiO_2/MnO_2$−PEG, degradation of MB was chosen as the model organic pollutant removal reaction. Figure 4A illustrates the degradation efficiencies for MB with $Cu_2O@SiO_2/MnO_2$−PEG under different conditions, with or without H_2O_2, $Cu_2O@SiO_2/MnO_2$−PEG, and visible light irradiation at wavelengths $\lambda \geq$ 420 nm. Virtually no degradation of MB occurred using just H_2O_2 or pure $Cu_2O@SiO_2/MnO_2$−PEG in the absence of light. The concentration of MB decreased by ~0.3% after an hour, which indicated little catalytic activity for the $Cu_2O@SiO_2/MnO_2$−PEG catalyst in the absence of an exogenous stimulus. However, $Cu_2O@SiO_2/MnO_2$−PEG showed effective catalytic activity in the presence of either H_2O_2 or visible light and reached MB degradation rates of 47.7% and 34.8% after 60 min, respectively. Subsequently, the catalytic activities of $Cu_2O@SiO_2/MnO_2$−PEG were investigated with both H_2O_2 and visible light irradiation, which resulted in MB degradation rates of 92.5% and 99.0% for 30 and 60 min reaction times, respectively. These results were attributed to MnO_2 Fenton−like catalytic and Cu_2O photocatalytic properties, through which reactive oxygen species (ROS) and electron−hole pairs were produced as the active reaction species, respectively (Watts et al., 2005; Furman et al., 2009). Furthermore, H_2O_2 acts as a good radical •OH generator because of its advantages in electron acceptor and facilitation in the separation of electron−hole pairs (Zhai et al., 2013). As a result, the integration of MnO_2 and Cu_2O promotes MB degradation efficiency under visible light and the presence of H_2O_2. Additionally, zeta potential of $Cu_2O@SiO_2/MnO_2$−PEG before and after adsorption equilibrium were −18.3 eV and −16.4 eV, respectively. No obvious change was observed.

Time−dependent UV−Vis absorption spectra measured MB solution concentrations using $Cu_2O@SiO_2/MnO_2$−PEG (see Figure 4B). The intensity of the MB absorption peak at 664 nm

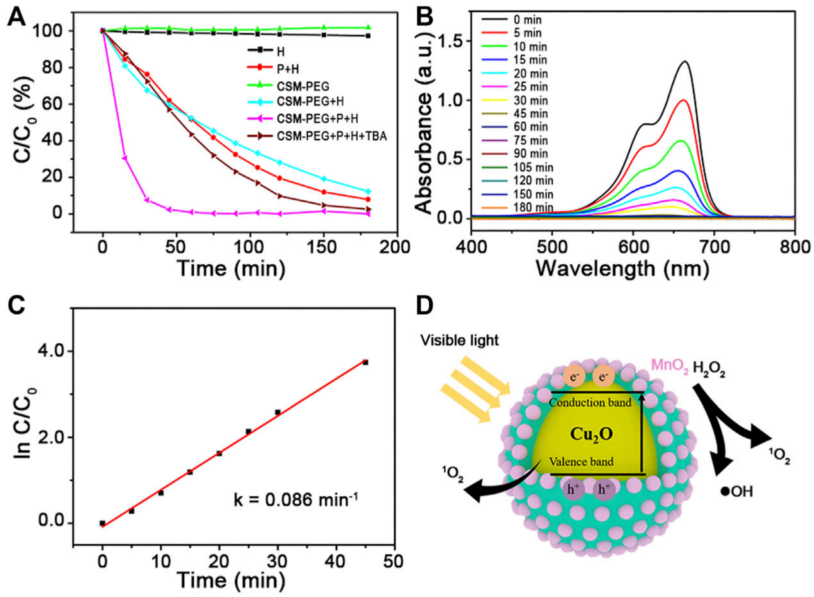

FIGURE 4
(A) Catalytic activities of $Cu_2O@SiO_2/MnO_2$–PEG for degradation of MB under different conditions. **(B)** UV–Vis spectra measured for the MB solution versus time in the presence of visible light and H_2O_2. **(C)** The kinetic fitting lines for H_2O_2–enhanced photodegradation of MB over $Cu_2O@SiO_2/MnO_2$–PEG (k = 0.086 min^{-1}). **(D)** Schematic illustration of MB degradation over $Cu_2O@SiO_2/MnO_2$–PEG under visible light.

TABLE 1 Catalytic performances of catalytic degradation of MB dye reported elsewhere.

Catalyst	Sample concentration (mg L^{-1})	Reaction conditions (MB concentration/mg L^{-1}; reaction time/min)	Exogenous conditions	Rate constant (10^{-3} min^{-1})	References
ZnO nanostructure	5	1.2; 150	UV light and H_2O_2	17.0	Mohammadzadeh et al. (2020)
TiO_2/ micro–cellulose	200	200; 150	Sunlight and H_2O_2	29.7	Rajagopal et al. (2020)
1–D $Cu(tba)_2(H_2O)]\cdot 2H_2O$	2000	10; 90	UV light and H_2O_2	22.2	Wang et al. (2020)
$ZnFe_2O_4/BiVO_4$	1500	40; 120	Visible light and H_2O_2	16.8	Cao et al. (2021)
Fe_3O_4@NIP	1000	25; 300	H_2O_2	9.4	Zhang et al. (2021b)
Hematite nanoplates	500	10; 120	Visible light and H_2O_2	4.3	Zong et al. (2021)
$C_{44}H_{68}FeN_3O_{10}$	73	60; 180	Visible light and H_2O_2	32.2	Dasgupta et al. (2014)
Fe_2O_3–TiO_2/GA	1000	50; 60	UV light and H_2O_2	55.8	Tu et al. (2020)
$Cu_2O@SiO_2/MnO_2$–PEG	150	10; 45	Visible light and H_2O_2	86.0	This research

declined significantly within the first 30 min. This behavior follows pseudo–first–order kinetics, and the value of the linear slope equals the degradation rate constant (Siddiqui et al., 2020). A plot of ln C/C_0 versus time (see Figure 4C) yielded an MB degradation rate constant of 0.086 min^{-1}. In comparison with previous studies, see Table 1, $Cu_2O@SiO_2/MnO_2$–PEG showed excellent catalytic activity at a sample concentration of 150 mg L^{-1} for MB degradation under visible light with H_2O_2 addition. In addition, it is generally

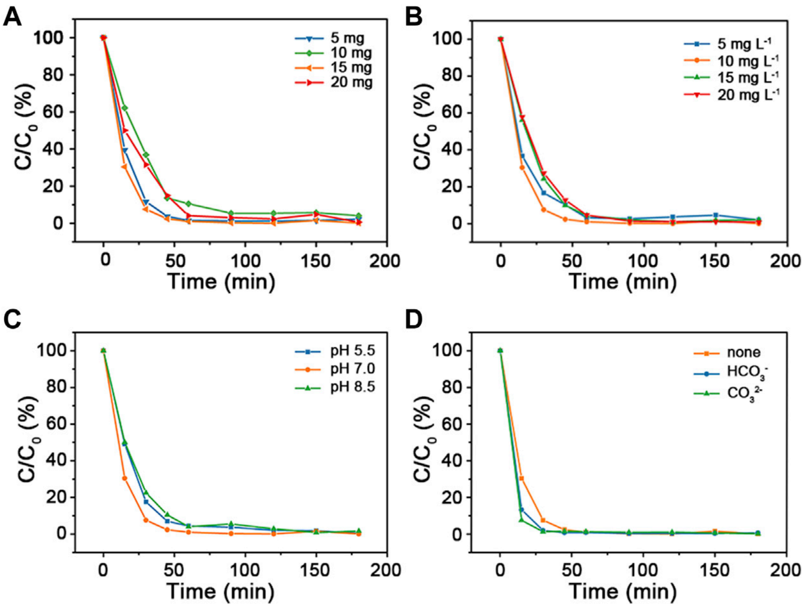

FIGURE 5
(A) Catalytic activities of $Cu_2O@SiO_2/MnO_2$–PEG for degradation of MB using various catalyst dosage (5 mg, 10 mg, 15 mg, and 20 mg). **(B)** Alteration of initial MB concentration (5 mg L^{-1}, 10 mg L^{-1}, 15 mg L^{-1}, and 20 mg L^{-1}) in MB degradation. **(C)** Changes of different pH environment adjusted by HCl and NaOH (pH = 5.5; 7.0, and 8.5) in MB degradation. **(D)** Catalytic performances of MB degradation co-existence of inorganic irons (HCO_3^- or CO_3^{2-}). Common experimental conditions: 15 mg of $Cu_2O@SiO_2/MnO_2$–PEG; 10 mg L^{-1} of MB concentration; pH = 7.0 of reaction solution without any other inorganic ion.

accepted that surface areas play a significant role in the photocatalytic activity of photocatalyst. For $Cu_2O@SiO_2/MnO_2$–PEG, the specific surface areas is 26.8 $m^2\ g^{-1}$, which was much higher than reported Cu–$BiVO_4$ (6.5 $m^2\ g^{-1}$). In addition, N_2 physical adsorption and desorption curves showed typical type IV isotherms with H3-type hysteresis loops, indicating the presence of slit-shaped mesopores formed by the stacking of nanoparticles (supporting information Supplementary Figure S2) (Xu et al., 2020). High surface areas would favor the initial adsorption of MB and providing additional accessible active sites, which benefit to enhance the activity of photocatalyst (Wang et al., 2017b). The schematic illustration of MB degradation under visible light over $Cu_2O@SiO_2/MnO_2$–PEG was shown in Figure 4D. In addition, the effects of reaction conditions on catalytic activity and possible mechanism of this reaction had been investigated and illustrated carefully in the following study.

3.3 Effects of reaction conditions on the degradation of MB

The influence of reaction conditions (such as catalyst dosage, MB concentration, pH value, and inorganic ions) were carried out. The results were shown in Figure 5. Degradation rate decreases with catalyst dosage increasing from 10 mg to 20 mg. This might be resulted from the agglomeration of $Cu_2O@SiO_2/MnO_2$–PEG, which resulted in decrement of active points on its surface. However, the degradation rate shows tiny difference for catalyst dosage variation of $Cu_2O@SiO_2/MnO_2$–PEG. In Figure 5B, with the increasement of MB concentration, the tendency of degradation rate first shows an upward trend and then decreases within 60 min. The 10 mg L^{-1} of MB status presents the highest degradation rate when MB concentration increased from 5 mg L^{-1}–20 mg L^{-1}. Additionally, the influence of pH on the photodegradation of MB value was evaluated from 5.5 to 8.5. See in Figure 5C, $Cu_2O@SiO_2/MnO_2$–PEG exibits better photocatalytic activity at pH = 7.0 than others. The pH affected the stability of catalyst, which would further affect the photocatalytic performances. In acid solution, MnO_2 reacted with H_2O_2 to Mn^{2+}. Meanwhile, •OH could be scavenged by OH^- under alkaline conditions, resulting in less •OH in MB solution (Liu et al., 2015). Therefore, the photocatalytic efficiency decreased with the variation of pH = 7. In fact, various inorganic ions may co-exist in dye wastewater. Herein, the effects of co-existing ions on MB degradation was examined. In current study, HCO_3^- (1500 mg L^{-1}) and CO_3^{2-} (1500 mg L^{-1}) were

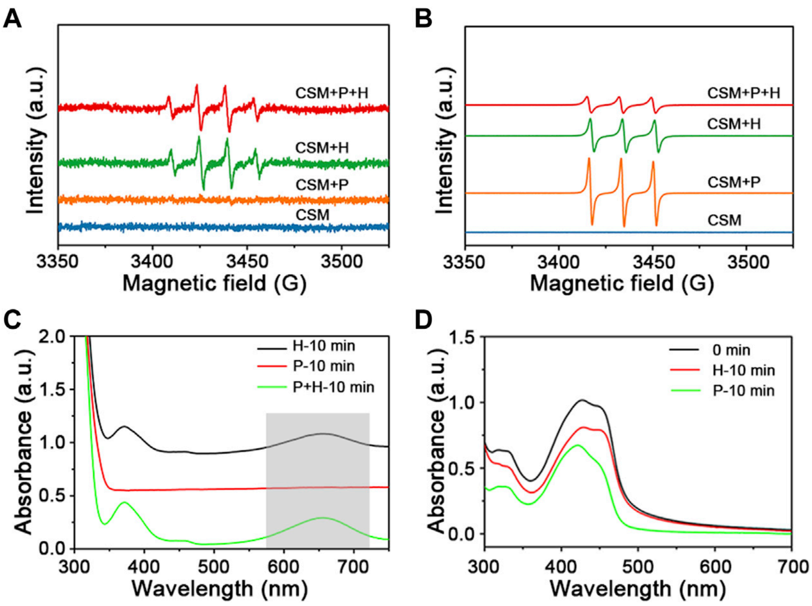

FIGURE 6
(A) EPR spectra of radical adduct trapped by DMPO-•OH with or without H_2O_2 (H) and visible light irradiation (P) over $Cu_2O@SiO_2/MnO_2$–PEG. **(B)** EPR spectra of radical adduct trapped by TEMPO-$^1O_2$. (labelled as "CSM + H", "CSM + P", and "CSM + P + H"). **(C)** UV–Vis spectra measuring of TMB in a reaction system with H_2O_2 and visible light over $Cu_2O@SiO_2/MnO_2$–PEG. **(D)** UV–Vis spectra measuring of DPBF with H_2O_2 or visible light stimuli.

chosen as the extra existence of irons. As shown in Figure 5D, no significant variable is observed in alterative test, which suggests that degradation is well stably controlled. Consequently, the descended removal efficiency would not be caused by the interaction of inorganic irons. As a result, 15 mg of catalyst dosage and 10 mg L^{-1} of MB concentration at pH = 7.0 environment were chosen as the optional experimental conditions. Finally, all of the MB dye was degraded totally.

3.4 Mechanism

To investigate the mechanism involved in the photodegradation of MB over $Cu_2O@SiO_2/MnO_2$–PEG, EPR is employed. 5,5-dimethly-1-pyrroline-Noxide (DMPO, 30 mmol L^{-1}) and 2,2,6,6-Tetramethyl-1-piperidinyloxy (TEMPO, 10 mmol L^{-1}) were used as the trapping agents of •OH and $^1O_2$, respectively. It was reported that the strong intensity peaks ratio of 1:2:2:1 and 1:1:1 would be classified to the formation of DMPO–•OH and TEMPO–$^1O_2$, respectively (Harbour et al., 1974; Ma et al., 2022). As shown in Figures 6A,B, there are no signals using $Cu_2O@SiO_2/MnO_2$–PEG alone. It can be observed that radical •OH was presented with H_2O_2 addition instead of visible light exposure over $Cu_2O@SiO_2/MnO_2$–PEG. Thus, the results indicated the importance role of H_2O_2 as the •OH generator. Comparably, $^1O_2$ was generated in the presence of H_2O_2 or visible light. Any of the two ways of stimuli is effective on $^1O_2$ generation. Finally, the co-stimuli of H_2O_2 and visible light may contribute to the high efficient degradation of MB over $Cu_2O@SiO_2/MnO_2$–PEG.

To confirm the possible mechanism for photo–Fenton–like degradation of MB, an •OH indicator (3,3′,5,5′–tetramethylbenzidine, TMB, 10 mg L^{-1}) and an $^1O_2$ indicator (1,3–diphenylisobenzofuran, DPBF, 2 mg L^{-1}) were added. As shown in Figure 6, the appearance of a peak at 652 nm indicated the reaction of •OH and TMB, and the intensity decrease of the peak at 425 nm demonstrated the reaction of $^1O_2$ and DPBF (Fan et al., 2015; Deng et al., 2019). Radical •OH only was generated during the catalytic decomposition of H_2O_2 *via* TMB testing (marked as "H" in Figure 6C). Meanwhile, both visible light and H_2O_2 stimuli generated $^1O_2$, the active species in the catalytic degradation of MB (see Figure 6D). Consequently, the results were exactly consistent with the EPR characterization.

According to the previous evaluation, the possible formation mechanism of main active radicals is as follows. First, owing to short lifetime and limited migration distance of •OH, reactions to generate $^1O_2$ readily occured (Eq. 3). Furthermore, •OH scavenger t–butanol (TBA, 0.1 g) was introduced into the reaction system, and the time–dependent curve (labeled "CSM–PEG + P + H + TBA") displayed a similar extension to the "P + H" curve (see Figure 4A). This result agreed with the results shown in Figure 5A, which confirmed the absence of •OH under visible light irradiation (Kang et al., 2019; Yan et al., 2021; Yang L. et al., 2022).

$$4\bullet OH \rightarrow {}^1O_2 + 2H_2O \quad (3)$$

Many e^- (CB) and h^+ (VB) pairs formed on the (Cu_2O) photosensitizer surface *via* visible light irradiation (Eq. 4). At the same time, MnO_2 catalyzed H_2O_2 to generate O_2, which combined with an electron to form an $O_2^{\bullet -}$ species (Eqs. 5, 6). Subsequently, $O_2^{\bullet -}$ generated ${}^1O_2$ as shown in Eq. 7 (Zhu et al., 2019; Rajagopal et al., 2020). Therefore, H_2O_2 benefited O_2 production, which resulted in significant amounts of ${}^1O_2$. Furthermore, due to PEG modification, many surface OH groups on $Cu_2O@SiO_2/MnO_2$ acted as hole traps, which facilitated the separation of electron–hole pairs and promoted •OH and ${}^1O_2$ production (Trandafilović et al., 2017).

$$Cu_2O \xrightarrow{hv} Cu_2O\left(h^+ + e^-\right) \quad (4)$$

$$H_2O_2 \xrightarrow{MnO_2} H_2O + O_2 \quad (5)$$

$$O_2 + e^- \rightarrow O_2^{\bullet -} \quad (6)$$

$$2O_2^{\bullet -} + 2H_2O \rightarrow {}^1O_2 + H_2O_2 + 2OH^- \quad (7)$$

$$\bullet OH/{}^1O_2 + MB \rightarrow \text{degraded products} \quad (8)$$

Ultimately, •OH and ${}^1O_2$ triggered the degradation of MB *via* the integration of radical and non–free radical pathways (Eq. 8). $Cu_2O@SiO_2/MnO_2$–PEG enhanced the catalytic degradation of MB by a photo–Fenton–like process over H_2O_2 under visible light irradiation.

4 Conclusion

$Cu_2O@SiO_2/MnO_2$–PEG, with a core–shell structure and an average 52 nm diameter, was synthesized and protected Cu_2O against oxidation *via* a dense SiO_2 shell. Integration of Cu_2O and MnO_2 united the photo–Fenton–like catalytic properties of $Cu_2O@SiO_2/MnO_2$–PEG in the presence of H_2O_2 under visible light. Additionally, a degradation rate of 92.5% and a rate constant of 0.086 min^{-1} were recorded for MB degradation in 30 min for a 10 mg L^{-1} MB solution, which indicated excellent catalytic activity of $Cu_2O@SiO_2/MnO_2$–PEG as compared to previous studies. MB degradation was well stably controlled, resulting from no significant change of catalytic performances after catalyst dosage, MB concentration, pH value, and inorganic ions variation. Based on EPR characterization and •OH and ${}^1O_2$ indicators, MB degradation proceeds *via* the integration of radical and non–free radical pathways. Thus, $Cu_2O@SiO_2/MnO_2$–PEG is a promising candidate for the degradation of dye pollutants sensitive to •OH and ${}^1O_2$. The growth mechanism in structure–oriented MnO_2 and its interaction with Cu_2O requires further exploration.

Data availability statement

The original contributions presented in the study are included in the article/Supplementary Material, further inquiries can be directed to the corresponding authors.

Author contributions

MW performed the experiments and wrote the manuscript. SH and EH discussed the results and revised the manuscript. JH discussed the results. SC supervised all the works. All authors listed contributed to the article and approved it for publication.

Funding

This research was funded the National Natural Science Foundation of China (grant numbers: 61935014, 51972055, 22004087, 21701135); the Shenzhen Pengcheng Scholar Program; the Guangdong Basic and Applied Basic Research Foundation (grant numbers: 2019A1515110926); the Natural Science Foundation of Top Talent of Shenzhen Technology University (grant numbers: 20200202); the Shenzhen Science and Technology Innovation Commission (grant number: JCYJ20180508152903208 and JCYJ20190809145601651).

Conflict of interest

The authors declare that the research was conducted in the absence of any commercial or financial relationships that could be construed as a potential conflict of interest.

Supplementary material

The Supplementary Material for this article can be found online at: https://www.frontiersin.org/articles/10.3389/fbioe.2022.1023090/full#supplementary-material

References

Alp, E. (2021). The Facile Synthesis of Cu_2O-Cu hybrid cubes as efficient visible-light-driven photocatalysts for water remediation processes. *Powder Technol.* 394, 1111–1120. doi:10.1016/j.powtec.2021.09.031

An, L., Wang, X., Rui, X., Lin, J., Yang, H., Tian, Q., et al. (2018). The *in situ* sulfidation of Cu_2O by endogenous H_2S for colon cancer theranostics. *Angew. Chem. Int. Ed.* 57 (48), 15782–15786. doi:10.1002/anie.201810082

Anwer, H., Mahmood, A., Lee, J., Kim, K.-H., Park, J.-W., and Yip, A. C. K. (2019). Photocatalysts for degradation of dyes in industrial effluents: Opportunities and challenges. *Nano Res.* 12 (5), 955–972. doi:10.1007/s12274-019-2287-0

Caccamo, M. T., and Magazù, S. (2017). Thermal restraint on PEG-EG mixtures by FTIR investigations and wavelet cross-correlation analysis. *Polym. Test.* 62, 311–318. doi:10.1016/j.polymertesting.2017.07.008

Cao, Y., Ren, Y., Zhang, J., Xie, T., and Lin, Y. (2021). Activation of H_2O_2 by photo-generated electrons for enhanced visible light driven methylene blue degradation with $ZnFe_2O_4/BiVO_4$ heterojunction. *Opt. Mat. (Amst).* 121, 111637. doi:10.1016/j.optmat.2021.111637

Cheng, L., Liu, W., Zhang, Z., Zhou, Y., and Li, S. (2022). Enhanced breakdown strength and restrained dielectric loss of polypropylene/maleic anhydride grafted polypropylene/core-shell $ZrO_2@SiO_2$ nanocomposites. *Polym. Compos.* 43, 2175–2183. doi:10.1002/pc.26530

Colón, G., Maicu, M., Hidalgo, M. C., and Navío, J. A. (2006). Cu-doped TiO_2 systems with improved photocatalytic activity. *Appl. Catal. B Environ.* 67 (1), 41–51. doi:10.1016/j.apcatb.2006.03.019

Dasgupta, S., Atta, S., Singh, N. D. P., Deb, D., Kassel, W. S., and Bhattacharjee, M. (2014). Synthesis and structure of $[Et_3NH]$ $[Fe(HL)_2]$ [H_3L = L-2-(3, 5-Di-tert-butyl-2-hydroxybenzylamino)succinic acid] and its catalytic activity towards efficient photodegradation of dyes in the presence of H_2O_2. *Eur. J. Inorg. Chem.* 2014 (30), 5125–5134. doi:10.1002/ejic.201402314

Deng, H.-H., Luo, B.-Y., He, S.-B., Chen, R.-T., Lin, Z., Peng, H.-P., et al. (2019). Redox recycling-triggered peroxidase-like activity enhancement of bare gold nanoparticles for ultrasensitive colorimetric detection of rare-earth Ce^{3+} ion. *Anal. Chem.* 91 (6), 4039–4046. doi:10.1021/acs.analchem.8b05552

Deng, S., Jothinathan, L., Cai, Q., Li, R., Wu, M., Ong, S. L., et al. (2021). FeO_x@GAC catalyzed microbubble ozonation coupled with biological process for industrial phenolic wastewater treatment: Catalytic performance, biological process screening and microbial characteristics. *Water Res.* 190, 116687. doi:10.1016/j.watres.2020.116687

Fan, B.-Y., Liu, H.-B., Wang, Z.-H., Zhao, Y.-W., Yang, S., Lyu, S.-Y., et al. (2021). Ferroelectric polarization-enhanced photocatalytic performance of heterostructured $BaTiO_3@TiO_2$ via interface engineering. *J. Cent. South Univ.* 28 (12), 3778–3789. doi:10.1007/s11771-021-4847-y

Fan, W., Bu, W., Shen, B., He, Q., Cui, Z., Liu, Y., et al. (2015). Intelligent MnO_2 nanosheets anchored with upconversion nanoprobes for concurrent pH-/H_2O_2-responsive UCL imaging and oxygen-elevated synergetic therapy. *Adv. Mat.* 27 (28), 4155–4161. doi:10.1002/adma.201405141

Furman, O., Laine, D. F., Blumenfeld, A., Teel, A. L., Shimizu, K., Cheng, I. F., et al. (2009). Enhanced reactivity of superoxide in Water−Solid matrices. *Environ. Sci. Technol.* 43 (5), 1528–1533. doi:10.1021/es802505s

Gemeay, A. H., El-Sharkawy, R. G., Mansour, I. A., and Zaki, A. B. (2008). Catalytic activity of polyaniline/MnO_2 composites towards the oxidative decolorization of organic dyes. *Appl. Catal. B Environ.* 80 (1), 106–115. doi:10.1016/j.apcatb.2007.11.014

Ghauri, Z. H., Islam, A., Qadir, M. A., Ghaffar, A., Gull, N., Azam, M., et al. (2022). Novel pH-responsive chitosan/sodium alginate/PEG based hydrogels for release of sodium ceftriaxone. *Mat. Chem. Phys.* 277, 125456. doi:10.1016/j.matchemphys.2021.125456

Ghodselahi, T., Vesaghi, M. A., Shafiekhani, A., Baghizadeh, A., and Lameii, M. (2008). XPS study of the $Cu@Cu_2O$ core-shell nanoparticles. *Appl. Surf. Sci.* 255 (52), 2730–2734. doi:10.1016/j.apsusc.2008.08.110

Hao, J., Qi, B., Wei, J., Li, D., and Zeng, F. (2021). A Z-scheme Cu_2O/WO_3 heterojunction for production of renewable hydrocarbon fuel from carbon dioxide. *Fuel* 287, 119439. doi:10.1016/j.fuel.2020.119439

Harbour, J. R., Chow, V., and Bolton, J. R. (1974). An electron spin resonance study of the spin adducts of OH and HO2 radicals with nitrones in the ultraviolet photolysis of aqueous hydrogen peroxide solutions. *Can. J. Chem.* 52 (20), 3549–3553. doi:10.1139/v74-527

He, Z., Xia, Y., Tang, B., and Su, J. (2017). Fabrication and photocatalytic property of magnetic $NiFe_2O_4/Cu_2O$ composites. *Mat. Res. Express* 4 (9), 095501. doi:10.1088/2053-1591/aa7cb8

Huang, R., Gao, P., Zhu, J., Zhang, Y., Chen, Y., Huang, S., et al. (2022). Insights into the pollutant electron property inducing the transformation of peroxymonosulfate activation mechanisms on manganese dioxide. *Appl. Catal. B Environ.* 317, 121753. doi:10.1016/j.apcatb.2022.121753

Ivanets, A., Prozorovich, V., Sarkisov, V., Roshchina, M., Grigoraviciute-Puroniene, I., Zarkov, A., et al. (2021). Effect of magnesium ferrite doping with lanthanide ions on dark-visible- and UV-driven methylene blue degradation on heterogeneous Fenton-like catalysts. *Ceram. Int.* 47 (21), 29786–29794. doi:10.1016/j.ceramint.2021.07.150

Jiao, C., Wei, N., Liu, D., Wang, J., Liu, S., Fu, F., et al. (2021). Sustainable Fenton-like degradation of methylene blue over MnO_2-loaded poly(amidoxime-hydroxamic acid) cellulose microrods. *Int. J. Biol. Macromol.* 193, 1952–1961. doi:10.1016/j.ijbiomac.2021.11.026

Kang, Y. G., Yoon, H., Lee, C. S., Kim, E. J., and Chang, Y. S. (2019). Advanced oxidation and adsorptive bubble separation of dyes using MnO_2-coated Fe_3O_4 nanocomposite. *Water Res.* 151, 413–422. doi:10.1016/j.watres.2018.12.038

Li, J., Sun, Z., He, M., Gao, D., Li, Y., and Ma, J. (2022a). Simple synthesis of Ag nanoparticles/Cu_2O cube photocatalyst at room temperature: Efficient electron transfer improves photocatalytic performance. *Inorg. Chem. Commun.* 138, 109200. doi:10.1016/j.inoche.2022.109200

Li, M., Li, Z., Yu, X., Wu, Y., Mo, C., Luo, M., et al. (2022b). FeN_4-doped carbon nanotubes derived from metal organic frameworks for effective degradation of organic dyes by peroxymonosulfate: Impacts of FeN_4 spin states. *Chem. Eng. J.* 431, 133339. doi:10.1016/j.cej.2021.133339

Liu, S., Wen, M., Huang, M., Wang, H., Chen, Z., and Yu, N. (2022). Nanoscale hematoporphrin-based frameworks for photo-sono synergistic cancer therapy via utilizing Al(III) as metal nodes rather than heavy metals. *J. Colloid Interface Sci.* 616, 23–33. doi:10.1016/j.jcis.2022.02.040

Liu, Y., He, X., Duan, X., Fu, Y., and Dionysiou, D. D. (2015). Photochemical degradation of oxytetracycline: Influence of pH and role of carbonate radical. *Chem. Eng. J.* 276, 113–121. doi:10.1016/j.cej.2015.04.048

Ma, W., Dong, X. a., Wang, Y., He, W., Zhang, W., Liang, Y., et al. (2022). Highly enhanced photocatalytic toluene degradation and *in situ* FT-IR investigation on designed Sn-doped BiOCl nanosheets. *Appl. Surf. Sci.* 578, 152002. doi:10.1016/j.apsusc.2021.152002

Mohammadzadeh, A., Khoshghadam-Pireyousefan, M., Shokrianfard-Ravasjan, B., Azadbeh, M., Rashedi, H., Dibazar, M., et al. (2020). Synergetic photocatalytic effect of high purity ZnO pod shaped nanostructures with H_2O_2 on methylene blue dye degradation. *J. Alloys Compd.* 845, 156333. doi:10.1016/j.jallcom.2020.156333

Mohammed, A. A., Atiya, M. A., and Hussein, M. A. (2020). Simultaneous studies of emulsion stability and extraction capacity for the removal of tetracycline from aqueous solution by liquid surfactant membrane. *Chem. Eng. Res. Des.* 159, 225–235. doi:10.1016/j.cherd.2020.04.023

Ni, T., You, Y., Xie, Z., Kong, L., Newman, B., Henderson, L., et al. (2022). Waste-derived carbon fiber membrane with hierarchical structures for enhanced oil-in-water emulsion separation: Performance and mechanisms. *J. Memb. Sci.* 653, 120543. doi:10.1016/j.memsci.2022.120543

Qiu, P., Huang, M., Wu, S., Wen, M., Yu, N., and Chen, Z. (2022). Dynamic effects of endo–exogenous stimulations on enzyme-activatable polymeric nanosystems with photo–sono–chemo synergy. *ACS Appl. Mat. Interfaces* 14 (26), 29537–29549. doi:10.1021/acsami.2c05276

Qiu, Y., Xu, X., Xu, Z., Liang, J., Yu, Y., and Cao, X. (2020). Contribution of different iron species in the iron-biochar composites to sorption and degradation of two dyes with varying properties. *Chem. Eng. J.* 389, 124471. doi:10.1016/j.cej.2020.124471

Rajagopal, S., Paramasivam, B., and Muniyasamy, K. (2020). Photocatalytic removal of cationic and anionic dyes in the textile wastewater by H_2O_2 assisted TiO_2 and micro-cellulose composites. *Sep. Purif. Technol.* 252, 117444. doi:10.1016/j.seppur.2020.117444

Siddiqui, H., Qureshi, M. S., and Haque, F. Z. (2020). Biosynthesis of flower-shaped CuO nanostructures and their photocatalytic and antibacterial activities. *Nano-Micro Lett.* 12 (1), 29. doi:10.1007/s40820-019-0357-y

Singh, K., Kumar, A., Pandey, S. K., Awasthi, S., Gupta, S. P., and Mishra, P. (2020). Interpretation of adsorption behavior of carboxymethyl cellulose onto functionalized accurel polymeric surface. *Ind. Eng. Chem. Res.* 59 (43), 19102–19116. doi:10.1021/acs.iecr.0c03894

Sun, X., Sun, J., Sun, Y., Li, C., Fang, J., Zhang, T., et al. (2021). Oxygen self-sufficient nanoplatform for enhanced and selective antibacterial photodynamic therapy against anaerobe-induced periodontal disease. *Adv. Funct. Mat.* 31 (20), 2101040. doi:10.1002/adfm.202101040

Trandafilović, L. V., Jovanović, D. J., Zhang, X., Ptasińska, S., and Dramićanin, M. D. (2017). Enhanced photocatalytic degradation of methylene blue and methyl orange by ZnO:Eu nanoparticles. *Appl. Catal. B Environ.* 203, 740–752. doi:10.1016/j.apcatb.2016.10.063

Tu, T. H., Tai, L. T., Tien, N. T., Huong, L. M., Oanh, D. T. Y., Nam, H. M., et al. (2020). Synthesis of Fe_2O_3/TiO_2/graphene aerogel composite as an efficient Fenton-photocatalyst for removal of methylene blue from aqueous solution. *Vietnam J. Chem.* 58 (5), 697–704. doi:10.1002/vjch.202000109

Uddin, M. J., Ampiaw, R. E., and Lee, W. (2021). Adsorptive removal of dyes from wastewater using a metal-organic framework: A review. *Chemosphere* 284, 131314. doi:10.1016/j.chemosphere.2021.131314

Wang, B., Wang, Y., Guo, X., Jiao, Z., Jin, G., and Guo, X. (2017a). Reduced graphene oxide supported Cu_2O nanoparticles as an efficient catalyst for Sonogashira coupling reaction. *Catal. Commun.* 101, 36–39. doi:10.1016/j.catcom.2017.07.020

Wang, C., Huang, R., Sun, R., Yang, J., and Sillanpää, M. (2021a). A review on persulfates activation by functional biochar for organic contaminants removal: Synthesis, characterizations, radical determination, and mechanism. *J. Environ. Chem. Eng.* 9 (5), 106267. doi:10.1016/j.jece.2021.106267

Wang, C., Sun, R., Huang, R., and Wang, H. (2021b). Superior fenton-like degradation of tetracycline by iron loaded graphitic carbon derived from microplastics: Synthesis, catalytic performance, and mechanism. *Sep. Purif. Technol.* 270, 118773. doi:10.1016/j.seppur.2021.118773

Wang, D., Zhao, P., Yang, J., Xu, G., Yang, H., Shi, Z., et al. (2020). Photocatalytic degradation of organic dye and phytohormone by a Cu(II) complex powder catalyst with added H_2O_2. *Colloids Surfaces A Physicochem. Eng. Aspects* 603, 125147. doi:10.1016/j.colsurfa.2020.125147

Wang, M., Guo, P., Chai, T., Xie, Y., Han, J., You, M., et al. (2017b). Effects of Cu dopants on the structures and photocatalytic performance of cocoon-like Cu-$BiVO_4$ prepared via ethylene glycol solvothermal method. *J. Alloys Compd.* 691, 8–14. doi:10.1016/j.jallcom.2016.08.198

Wang, Z., Zhang, Y., Ju, E., Liu, Z., Cao, F., Chen, Z., et al. (2018). Biomimetic nanoflowers by self-assembly of nanozymes to induce intracellular oxidative damage against hypoxic tumors. *Nat. Commun.* 9 (1), 3334. doi:10.1038/s41467-018-05798-x

Watts, R. J., Sarasa, J., Loge, F. J., and Teel, A. L. (2005). Oxidative and reductive pathways in manganese-catalyzed fenton's reactions. *J. Environ. Eng.* 131131 (1), 1581–2164. doi:10.1061/(asce)0733-9372(2005)131:1(158)

Weinberg, Z. A., Rubloff, G. W., and Bassous, E. (1979). Transmission, photoconductivity, and the experimental band gap of thermally grown SiO_2 films. *Phys. Rev. B* 19 (6), 3107–3117. doi:10.1103/PhysRevB.19.3107

Wu, G., Zhai, W., Sun, F., Chen, W., Pan, Z., and Li, W. (2012). Morphology-controlled electrodeposition of Cu_2O microcrystalline particle films for application in photocatalysis under sunlight. *Mat. Res. Bull.* 47 (12), 4026–4030. doi:10.1016/j.materresbull.2012.08.067

Xiong, Z., Huang, Y., Huang, Z., Shi, Y., Qu, F., Zhang, G., et al. (2022). Confining nano-Fe_3O_4 in the superhydrophilic membrane skin layer to minimize internal fouling. *ACS Appl. Mat. Interfaces* 14 (22), 26044–26056. doi:10.1021/acsami.2c04685

Xu, C., Shi, S., Wang, X., Zhou, H., Wang, L., Zhu, L., et al. (2020). Electrospun SiO2-MgO hybrid fibers for heavy metal removal: Characterization and adsorption study of Pb(II) and Cu(II). *J. Hazard. Mat.* 381, 120974. doi:10.1016/j.jhazmat.2019.120974

Yan, Q., Lian, C., Huang, K., Liang, L., Yu, H., Yin, P., et al. (2021). Constructing an acidic microenvironment by MoS_2 in heterogeneous fenton reaction for pollutant control. *Angew. Chem. Int. Ed.* 60 (31), 17155–17163. doi:10.1002/anie.202105736

Yang, J., Huang, R., Wang, L., Luo, D., and Wang, C. (2022a). Efficient degradation of toxic mixed dyes through peroxymonosulfate activation by copper/iron nanoparticles loaded on 3D carbon: Synthesis, characterizations, and mechanism. *J. Environ. Chem. Eng.* 10 (3), 107606. doi:10.1016/j.jece.2022.107606

Yang, L., Jiao, Y., Xu, X., Pan, Y., Su, C., Duan, X., et al. (2022b). Superstructures with atomic-level arranged perovskite and oxide layers for advanced oxidation with an enhanced non-free radical pathway. *ACS Sustain. Chem. Eng.* 10 (5), 1899–1909. doi:10.1021/acssuschemeng.1c07605

Yang, R., Fan, Y., Ye, R., Tang, Y., Cao, X., Yin, Z., et al. (2021). MnO_2-Based materials for environmental applications. *Adv. Mat.* 33 (9), 2004862. doi:10.1002/adma.202004862

Yang, Y., Xu, D., Wu, Q., and Diao, P. (2016). Cu_2O/CuO bilayered composite as a high-efficiency photocathode for photoelectrochemical hydrogen evolution reaction. *Sci. Rep.* 6 (1), 35158. doi:10.1038/srep35158

Yu, N., Qiu, P., Ren, Q., Wen, M., Geng, P., Macharia, D. K., et al. (2021a). Transforming a sword into a knife: Persistent phototoxicity inhibition and alternative therapeutical activation of highly-photosensitive phytochlorin. *ACS Nano* 15 (12), 19793–19805. doi:10.1021/acsnano.1c07241

Yu, N., Tu, W., Qiu, P., Ren, Q., Chen, X., Zhu, M., et al. (2022). Full-route advances via biomimetic and biodegradable ultrasmall-in-nano architectures with radiation-photo synergy. *Nano Today* 43, 101427. doi:10.1016/j.nantod.2022.101427

Yu, N., Wang, Z., Zhang, J., Liu, Z., Zhu, B., Yu, J., et al. (2018). Thiol-capped Bi nanoparticles as stable and all-in-one type theranostic nanoagents for tumor imaging and thermoradiotherapy. *Biomaterials* 161, 279–291. doi:10.1016/j.biomaterials.2018.01.047

Yu, X., Zhang, J., Chen, Y., Ji, Q., Wei, Y., Niu, J., et al. (2021b). Ag-Cu_2O composite films with enhanced photocatalytic activities for methylene blue degradation: Analysis of the mechanism and the degradation pathways. *J. Environ. Chem. Eng.* 9 (5), 106161. doi:10.1016/j.jece.2021.106161

Zhai, W., Sun, F., Chen, W., Zhang, L., Min, Z., and Li, W. (2013). Applications of Cu_2O octahedral particles on ITO glass in photocatalytic degradation of dye pollutants under a halogen tungsten lamp. *Mat. Res. Bull.* 48 (11), 4953–4959. doi:10.1016/j.materresbull.2013.07.034

Zhai, Z., Guo, X., Jiao, Z., Jin, G., and Guo, X.-Y. (2014). Graphene-supported Cu_2O nanoparticles: An efficient heterogeneous catalyst for C–O cross-coupling of aryl iodides with phenols. *Catal. Sci. Technol.* 4 (12), 4196–4199. doi:10.1039/C4CY01048E

Zhang, D.-F., Zhang, H., Shang, Y., and Guo, L. (2011). Stoichiometry-controlled fabrication of Cu_xS hollow structures with Cu_2O as sacrificial templates. *Cryst. Growth Des.* 11 (9), 3748–3753. doi:10.1021/cg101283w

Zhang, D. F., Zhang, H., Guo, L., Zheng, K., Han, X. D., and Zhang, Z. (2009). Delicate control of crystallographic facet-oriented Cu_2O nanocrystals and the correlated adsorption ability. *J. Mat. Chem.* 19 (29), 5220–5225. doi:10.1039/B816349A

Zhang, X., Li, C., Chen, T., Tan, Y., Liu, X., Yuan, F., et al. (2021a). Enhanced visible-light-assisted peroxymonosulfate activation over MnFe2O4 modified g-C3N4/diatomite composite for bisphenol A degradation. *Int. J. Min. Sci. Technol.* 31 (6), 1169–1179. doi:10.1016/j.ijmst.2021.11.008

Zhang, X., Wu, H., Ke, Z., Yang, J., Chen, H., Xue, F., et al. (2021b). A new effective way to degrade methylene blue by introducing negative ions powder into Fe_3O4/H_2O_2 system to accelerate Fe(III)/Fe(II) transformation. *Water Sci. Technol.* 83 (8), 1834–1846. doi:10.2166/wst.2021.097

Zhu, S., Li, X., Kang, J., Duan, X., and Wang, S. (2019). Persulfate activation on crystallographic manganese oxides: Mechanism of singlet oxygen evolution for nonradical selective degradation of aqueous contaminants. *Environ. Sci. Technol.* 53 (1), 307–315. doi:10.1021/acs.est.8b04669

Zong, M., Song, D., Zhang, X., Huang, X., Lu, X., and Rosso, K. M. (2021). Facet-dependent photodegradation of methylene blue by hematite nanoplates in visible light. *Environ. Sci. Technol.* 55 (1), 677–688. doi:10.1021/acs.est.0c05592